



Title	Color-coded visualization of microbubble clouds interacting with eddies in a spatially developing turbulent boundary layer
Author(s)	Park, Hyun Jin; Saito, Daichi; Tasaka, Yuji; Murai, Yuichi
Citation	Experimental thermal and fluid science, 109, UNSP 109919 <a href="https://doi.org/10.1016/j.expthermflusci.2019.109919">https://doi.org/10.1016/j.expthermflusci.2019.109919</a>
Issue Date	2019-12
Doc URL	<a href="http://hdl.handle.net/2115/83367">http://hdl.handle.net/2115/83367</a>
Rights	© 2019. This manuscript version is made available under the CC-BY-NC-ND 4.0 license <a href="http://creativecommons.org/licenses/by-nc-nd/4.0/">http://creativecommons.org/licenses/by-nc-nd/4.0/</a>
Rights(URL)	<a href="http://creativecommons.org/licenses/by-nc-nd/4.0/">http://creativecommons.org/licenses/by-nc-nd/4.0/</a>
Type	article (author version)
File Information	ETFS2019_MB_Revised_New_HUSCAP.pdf



[Instructions for use](#)

# 1 Color-coded visualization of microbubble clouds interacting with 2 eddies in a spatially developing turbulent boundary layer

3 Hyun Jin Park\*, Daichi Saito, Yuji Tasaka, Yuichi Murai

4 Laboratory for Flow Control, Faculty of Engineering, Hokkaido University, N13-W8, Kita-ku, Sapporo  
5 0608628, Japan

6 \* Corresponding author. Tel/fax: +81 11 706 6373, E-mail address: [park@eng.hokudai.ac.jp](mailto:park@eng.hokudai.ac.jp).

## 7 **Highlights**

- 8 • Turbulent eddy–microbubble interaction is investigated by two visualization methods.
- 9 • Microbubbles in a boundary layer are 3-dimensionally visualized by color illumination.
- 10 • These bubbles are accumulated in a vortical core by pressure gradient in the vortex.
- 11 • Also, streamwise vortices in a boundary layer are investigated by flake visualization method.
- 12 • Span-distance between vortices is increased by microbubbles injected into the layer.

## 13 **Abstract**

14 Three-dimensional distribution of microbubbles dispersed in a turbulent boundary layer spatially  
15 developing along a flat plate is investigated experimentally. The aim of study is to find out visually  
16 how microbubbles interact with turbulent eddies to achieve frictional drag reduction on a wall.  
17 Setting conditions of the experiments are stream Reynolds number up to  $2.3 \times 10^4$ , microbubble  
18 volume fraction inside boundary layer less than  $10^{-5}$ , and microbubble Stokes number smaller than  
19  $10^{-3}$ . Stream-wise vortices in the boundary layer were visualized by flake optics, of which spacing  
20 expands with injection of microbubbles. 3-D microbubble distributions were visualized by a color-  
21 coded volumetric illumination. The result showed preferentially accumulated microbubble clouds to  
22 low-speed streaks close to viscous sublayer and to hair-pin vortices in the buffer layer, leading to  
23 reduced diffusivity of microbubbles relative to the turbulent momentum diffusivity.

24 **Keywords;** Drag reduction, Microbubbles, Turbulent boundary layer, Flow visualization

## 25 **1. Introduction**

26 Microbubbles injected into turbulent boundary layers can reduce skin frictional drag acting on a solid surface.  
27 This is a known fact since 1973 as McCormick and Bhattacharyya [1] obtained a significant degree of drag  
28 reduction by generating microbubbles around a submerged hull in water flow. Legner [2] explained the  
29 reduction with shear-thickening trend of viscous sub-layer as microbubbles increase local effective viscosity.

1 Marie [3] attributed the reduction to decrease of Reynolds shear stress in the buffer layer with their  
2 accumulations. Question is where microbubbles tend to be accumulated inside turbulent boundary layers.  
3 Since 1990, many investigators tried to solve this experimentally with changing bubble size [4–8]. In these  
4 papers, the term of “microbubbles” was used in their paper title as a qualitative sense while actual size of the  
5 bubbles was ranged from 0.1 to 3.0 mm, called “milli-bubbles” but not in  $\mu\text{m}$  order. Such milli-bubbles in  
6 turbulent boundary layers of water show high bubble deformability in most applications [9]. Role of the  
7 deformability in shear stress field was reported by Tasaka *et al.* [10] for unsteady laminar flows, and by van  
8 Gils *et al.* [11] for high-speed turbulent flows. In these regime, Capillary number or Weber number  
9 characterizes the modification of shear stress field. Further large bubbles in Froude number dependence  
10 regime, formation of gas film and wettability sway the wall shear stress as reported by Park *et al.* [12] and  
11 Kitagawa *et al.* [13].

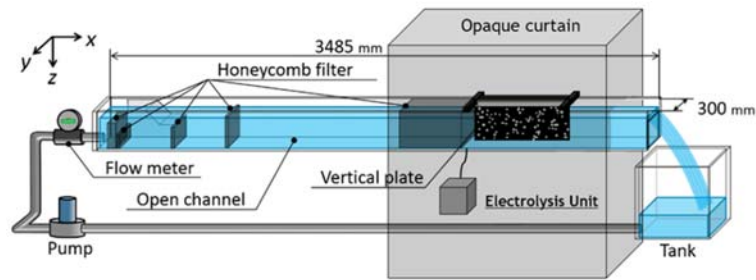
12 In contrast, bubbles smaller than 100  $\mu\text{m}$ , *i.e.*, actually  $\mu\text{m}$ -order bubbles, keep spherical shape without  
13 deformability in water up to 8 m/s in flow speed. In CFD studies, such tiny bubbles are approximated as  
14 point-source dispersions and called also “microbubbles” being distinguished from deformable bubbles.  
15 Ferrante and Elghobashi [14] conducted DNS on microbubble-laden wall turbulence and found that  
16 microbubbles pushed streamwise vortices away from the wall. One of unsolved issues is a role of generation  
17 of microbubble clouds. Once the clouds are formed, microbubbles cannot be directly simulated under the  
18 assumption of point source. Inside such a cloud, volume fraction and interfacial concentration rise sharply to  
19 modify local fluid properties such as density, viscosity and viscoelasticity [15, 16, 17]. The generation is  
20 promoted as the slip velocity of microbubbles to liquid phase is rather small. This is explained by comparison  
21 with milli-bubbles crossing over the coherent structures of turbulence. As Mathai *et al.* [18] reported,  
22 microbubbles induce preferential concentration in turbulence even at Stokes number is sufficiently low. In  
23 experimental approach, effect of microbubbles on turbulent shears was reported by many researchers [19–  
24 24]. Their experiments observed a high sensitivity to drag reduction or suppression of turbulence even in low  
25 bulk volume fraction of microbubbles. A key to explain the mechanism is to clarify where and how such  
26 microbubbles form clouds inside the boundary layers.

27 In the present experimental study, first, we show how the spatial distribution of coherent structure is  
28 altered with mixing of microbubbles. And then we investigate spatial distribution of microbubbles in the  
29 same situation. For the microbubble distribution inside the turbulent boundary layer, we have employed a  
30 three-dimensional (3-D) visualizing method. This method relies on volumetric illumination of microbubbles  
31 using a color-coded light projected in a wall proximity. The optical set-up requires only a single camera and  
32 it allows effective measurement volume to be kept large enough covering the whole boundary layer thickness.  
33 Similar technique was reported by Watamura *et al.* [24] and Xiong *et al.* [25] for tracer particles as a 3-D  
34 particle tracking velocimetry. With this method, it is presented how microbubbles form specific distributions  
35 during their two-way interactions between microbubbles and inner structures of wall turbulence.

1 **2. Experimental Method**

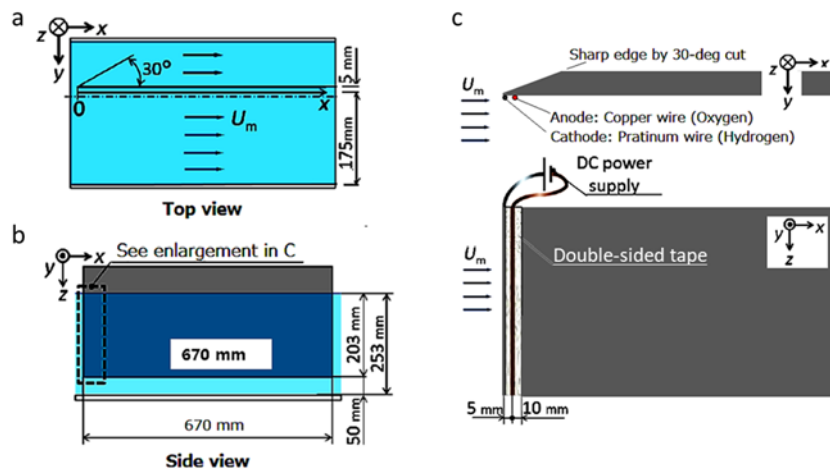
2 **2-1. Experimental facility**

3 A schematic diagram of experimental facility is shown in **Fig. 1**. It consists of an open water horizontal  
 4 channel of 3,485 mm in total length, a test plate set vertically in the downstream region of the channel, and  
 5 recirculation units including a pump, a flowmeter, and a bubble separating reservoir tank. The open channel  
 6 around the test plate is made of transparent acrylic resin for all the three sides to allow various optical  
 7 visualizations. And it is covered with opaque shading curtains to block light from outside.



8  
 9 **Fig. 1** Open channel facility for visualizing flat-plate turbulent boundary layer with microbubbles

10 The test plate is made of dielectric resin, which is 670 mm in stream-wise length, and 5 mm in thickness  
 11 as depicted in **Fig. 2a**. During the experiment, the test plate is submerged into water flow at a controlled  
 12 height (see **Fig. 2b**). Front of the plate is cut by 30° at the backside of the flat surface forming a sharp edge  
 13 to ensure parallel inflow as the starting point of a spatially developing boundary layer (see **Fig. 2c**). Four  
 14 honeycomb filters are set inside the open channel to produce uniform inflow with sufficiently small  
 15 turbulence intensity. The coordinate system is defined as the  $x$  axis in the streamwise direction, the  $y$  axis in  
 16 the direction away from the plate surface, and the  $z$  axis vertical.



17  
 18 **Fig. 2** Geometric set of wire electrodes at the front edge of a flat plate inserted in the open water channel;  
 19 (a) top view of the plate, (b) side view and (c) details of electrodes arrangement

1 For generating microbubbles by water electrolysis, tap water of  $0.5 \text{ m}^3$  in total volume is used as liquid  
 2 phase. At the front edge of the plate, a platinum wire of  $0.50 \text{ mm}$  in diameter as cathode and a copper wire  
 3 of  $0.45 \text{ mm}$  in diameter as anode are attached in parallel to the  $z$  axis with displacement of  $5 \text{ mm}$  (see **Fig.**  
 4 **2c**). Hydrogen gas released from the cathode as microbubbles is naturally conveyed into the boundary layer.  
 5 **Table 1** specifies the experimental conditions of microbubble generation. Diameter of the microbubbles  $d$  is  
 6 ranged from  $10$  to  $50 \text{ }\mu\text{m}$ , taking peak at  $30 \text{ }\mu\text{m}$ , which is much smaller than the boundary layer thickness,  
 7  $O(10 \text{ mm})$ . The electrode wires also have a role of tripping wires to initiate perturbation leading flow  
 8 transitions to ensure development of a turbulent boundary layer.

9 **Table 1** Experimental conditions for microbubble generation

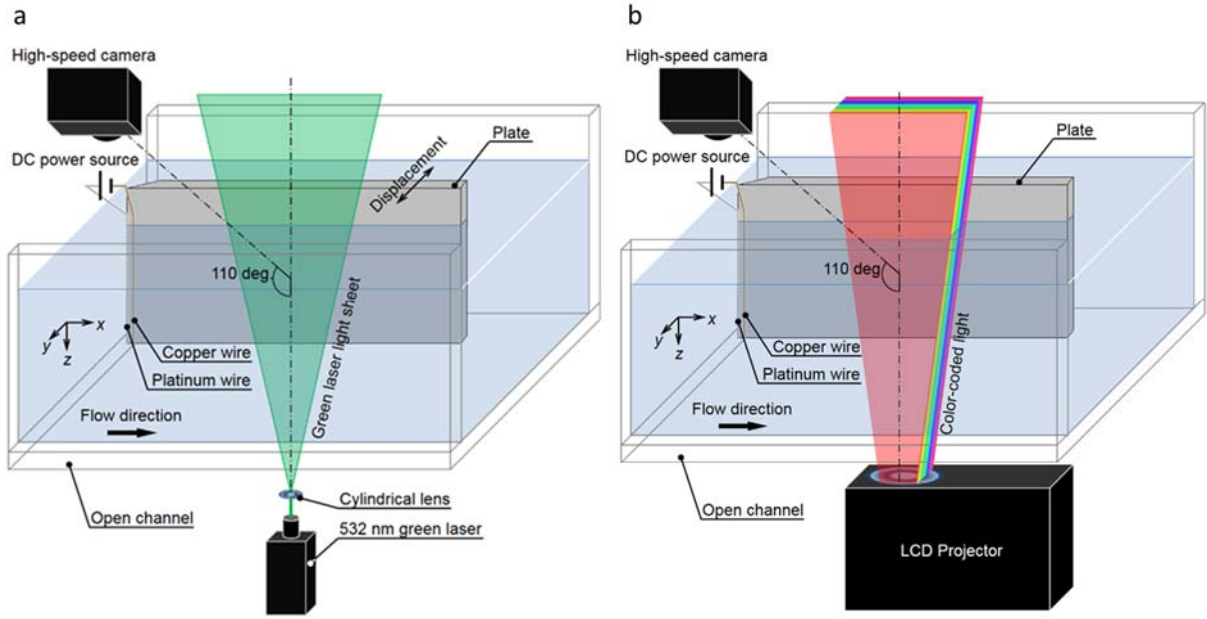
Electric current ( $J$ )	0.08–0.10	[A]
Mean inflow velocity of water ( $U_m$ )	67.1	[mm/s]
Temperature of water ( $T$ )	26.5–28.0	[°C]
Kinematic viscosity of water ( $\nu$ )	$0.839\text{--}0.868 \times 10^{-6}$	[m <sup>2</sup> /s]
Environmental pressure ( $P$ )	101.3–102.2	[kPa]
Diameter of hydrogen microbubble ( $d$ )	$30 \pm 20$	[ $\mu\text{m}$ ]
Flow rate of hydrogen bubble volume ( $Q_b$ )	$10.1\text{--}12.6 \times 10^{-9}$	[m <sup>3</sup> /s]
Liquid volume flow rate inside boundary layer ( $Q_l$ )	$0.172 \times 10^{-3}$	[m <sup>3</sup> /s]

## 10 2-2. Method of visualization

11 Two different types of optical visualization are conducted to measure alteration of turbulent coherent  
 12 structures and 3-D distributions of microbubbles as illustrated in Fig. 3.

13 For visualizing turbulent vortical structures in liquid phase, a flake aqueous solution (Kalliroscope AQ-  
 14 1000, Kalliroscope Ltd.) is mixed into water. The flakes have  $30 \times 6 \times 0.07 \text{ }\mu\text{m}^3$  in typical size, transparent  
 15 crystal structure of 1.85 of refractive optical index, and  $1.62 \times 10^3 \text{ kg/m}^3$  in density [26]. They reflect light as  
 16 like crushed mirrors dispersed, and therefore, parallel incident light to the flow visualizes the spatial  
 17 structure of turbulence [27]. This allows us to observe turbulent structure directly using the flakes without  
 18 any PIV analysis. More details will be explained in Section 3-1. Amount of the solution mixed is  $150 \text{ ml}$  in  
 19 total corresponding to  $300 \text{ ppm}$  in volume mixture rate (note that crystal solid volume fraction in the solution  
 20 is 0.1 of this value). Up to this solution rate, non-Newtonian viscosity does not take place as shear rate is  
 21 lower than  $10^2 \text{ s}^{-1}$ . As a source of light sheet,  $532 \text{ nm}$  continuous wave green laser with  $3 \text{ mm}$  in thickness is  
 22 used to illuminate the flake in the vicinity of the plate as shown in **Fig. 3a**. A high-speed camera (CamRecord  
 23 CR600x2, NAC Image Technology Inc.) set in front of the plate perpendicularly recorded the visualized  
 24 images at  $500 \text{ fps}$ .

1 For visualizing microbubble clouds, a color-coded volumetric light is illuminated closely to the wall using  
 2 a liquid crystal display projector (LCDP) as shown in **Fig. 3b**. Images are recorded by a high-speed video  
 3 camera (FASTCAM Mini AX-50, PHOTRON Ltd.) having color image sensors at frame rate of 500 fps. In  
 4 almost cases of the visualization, the camera is set with right angle,  $90^\circ$ , to visualized plane. In our  
 5 visualization, however, angle of optical axis of the volumetric light to the camera axis is set at  $110^\circ$  as shown  
 6 in the figure. Around this angle, between  $110^\circ$  and  $115^\circ$ , it is possible to obtain brightest scattering image of  
 7 microbubbles along Mie scattering principle of spherical bubbles [28].



8  
 9 **Fig. 3** Experimental setup for visualizing microbubble-laden flat-plate turbulent boundary layer in water;  
 10 (a) laser sheet illumination for visualizing turbulent vortical structures in liquid phase vicinity to the wall  
 11 and (b) optical set-up for microbubble visualization using color-coded volumetric illumination

### 12 2-3. Primary parameters in the experiments

13 There are two kinds of Reynolds numbers which signify flow structures of the present boundary layer:

$$14 \quad Re_x = \frac{U_m x}{\nu}, \quad (1)$$

$$15 \quad Re_f = \frac{u_\tau \delta}{\nu}, \quad u_\tau = \sqrt{\frac{\tau_w}{\rho}}, \quad (2)$$

16 where  $U_m$  is mean inflow velocity of water to the test plate in the open channel, and  $\nu$  is kinematic viscosity  
 17 of water without microbubbles. The first definition,  $Re_x$ , termed stream Reynolds number, increases with the  
 18 downstream distance,  $x$ . It takes the range up to  $Re_x = 2.3 \times 10^4$ .  $Re_f$  in Eq. (2) defines frictional Reynolds  
 19 number based on wall friction velocity,  $u_\tau$ , and boundary layer thickness,  $\delta$ , and it takes the range of  $50 < Re_f$

1 < 150 in this study, where  $\tau_w$  and  $\rho$  are wall friction and density of water. Basically, these two Reynolds  
 2 numbers are not independent of each other and show similar tendency because  $U_f$  and  $\delta$  are increasing with  
 3  $x$  in this situation.

4 For microbubble phase, following dimensionless parameters represent their status of motion:

$$5 \quad Re_b = \frac{U_b d}{\nu}, \quad (3)$$

$$6 \quad Re'_b = \frac{U'_\delta d}{\nu}, \quad (4)$$

$$7 \quad Ca = \frac{\mu \dot{\gamma} d}{\sigma} \square \frac{\mu d}{\sigma} \left( 7 \frac{U_m}{\delta} \right), \quad (5)$$

$$8 \quad St = \frac{u_\tau d^2}{36 \nu l_\tau} = \frac{\tau_w d^2}{36 \nu^2 \rho}, \quad l_\tau = \frac{\nu}{u_\tau}, \quad (6)$$

9 where  $\mu$ ,  $\dot{\gamma}$ ,  $\sigma$ ,  $d$ ,  $U_b$ ,  $U'_\delta$  and  $l_\tau$  denote viscosity of water, liquid shear rate of surrounding bubbles, interfacial  
 10 tension of bubbles, mean bubble diameter, free rising velocity of a single microbubble in quiescent water,  
 11 velocity fluctuation of flow in the boundary layer and wall unit, respectively. In the experiment, microbubble  
 12 Reynolds number with  $U_b$ ,  $Re_b$  in Eq. (3), takes the range of  $0.1 < Re_b < 1$ , *i.e.* in Stokes to Oseen regime. Eq.  
 13 (4) represents microbubble Reynolds number defined by the boundary layer velocity fluctuation  $U'_b$ , which  
 14 is  $Re'_b \leq 0.1$ .  $Ca$  in Eq. (5) defines microbubble Capillary number which is  $Ca < 10^{-4}$  in the present condition,  
 15 ensuring that microbubbles keep spherical shape. Here representative shear rate is given by liquid shear rate  
 16 on the wall obeying 1/7 power law as an estimate.  $St$  in Eq. (6) stands for microbubble Stokes number which  
 17 estimates the ratio of inertia response times of microbubble and of liquid phase in the boundary layer. In the  
 18 experiment, it is always in  $St \leq 0.001$ .

19 As a representative definition of volume fraction of the microbubble inside boundary layer, following  
 20 estimation is used:

$$21 \quad \alpha = \frac{Q_b}{Q_b + Q_l}, \quad Q_b = \frac{JRT}{2FP}, \quad Q_l = W \int_0^{\delta-} u(y) dy \square \frac{7}{8} W \delta U_m, \quad (7)$$

22 where volume flow rate of the microbubbles  $Q_b$  is given by Faraday law of water electrolysis:  $J$ ,  $R$ ,  $T$ ,  $F$  and  
 23  $P$  represent electric current, gas constant, temperature, Faraday constant, and pressure inside the gas phase,  
 24 respectively. Flow rate of the liquid phase inside the boundary layer  $Q_l$  is estimated by the 1/7 power law  
 25 about the velocity profiles, where  $W$  is the span-wise length of the plate. Present experiment takes the rage  
 26 of  $\alpha < 0.01\%$  (note that local volume fraction takes 2–3 digits higher value as microbubble clouds are formed).  
 27 We also note that wall unit takes the range of  $50 \mu\text{m} < l_\tau < 200 \mu\text{m}$  in our experiment. Thus, diameter of the  
 28 microbubbles,  $30 \mu\text{m}$ , is comparable with or smaller than the wall unit in this study.

### 1 3. Alternation of turbulent eddies

2 For high concentration of microbubbles in turbulent boundary layer, optical access such as PIV and LDV to  
3 the liquid velocity profile measurement is severely restricted. An alternative way to approach the liquid phase  
4 is flake optics that can directly visualize coherent structures in liquid phase. According to the previous studies  
5 [29–31], relationship between mean span-wise spacing of low-speed streaks  $\bar{\lambda}$  and the wall shear stress  $\tau_{\text{wall}}$   
6 is represented as

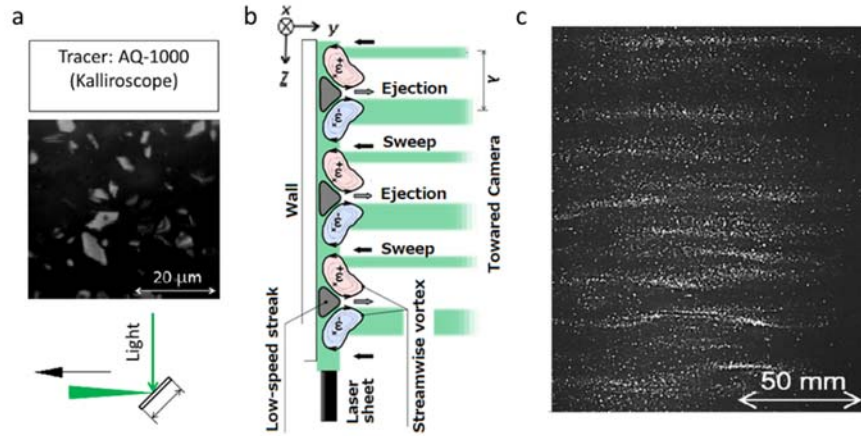
$$7 \quad \bar{\lambda} = a l_{\tau} \propto 1/\sqrt{\tau_{\text{wall}}} \rightarrow \frac{\tau_{\text{wall}}}{\tau_{\text{wall},0}} = \left( \frac{\bar{\lambda}}{\bar{\lambda}_0} \right)^{-2}, \quad (8)$$

8 where  $a$  is a dimensionless proportional constant to the wall unit  $l_{\tau}$  ranged at  $80 < a < 120$ . Hence,  
9 measurement of  $\bar{\lambda}$  in two cases with and without microbubble injection allows us to estimate how the wall  
10 shear stress is modified.

#### 11 3-1. Flake optics test

12 To visualize turbulent vortical structures, flake aqueous solution is mixed in the water channel (product name:  
13 Kalliroscope (AQ-1000)), which consists thin platelets made of Guanine ( $\text{C}_5\text{H}_5\text{N}_5\text{O}$ ) in crystalized state. The  
14 thickness of the platelet is about 10 nm while the width is less than 10  $\mu\text{m}$  as shown in **Fig. 4a**. The optical  
15 characteristics of the flake are available in our previous papers by Murai *et al.* [19] and Ohkubo *et al.* [27].  
16 As in shear flows, the platelets orient to the primary strain rate direction, and reflect light to mirror direction  
17 so that instantaneous spatial structure of turbulent boundary layer can be visualized. **Fig. 4b** is a schematic  
18 for explaining the optical principle applied for the turbulent boundary layer [32]. This set-up visualizes  
19 arrayed pair of stream-wise vortices and low-speed streaks as green separated bands in imaging plane. For  
20 ejection part, a thick reflection band appears just in front of the part. Inside sweep event, a thin reflection line  
21 appears in front of the sweep, asymmetrically. Park *et al.* [33] applied similar technique for a horizontal  
22 turbulent channel flows using aluminum flakes of larger than 100  $\mu\text{m}$  in size. We employ the technique using  
23 Kalliroscope so that flake does not disturb microbubble motions both in individual and clouded states.

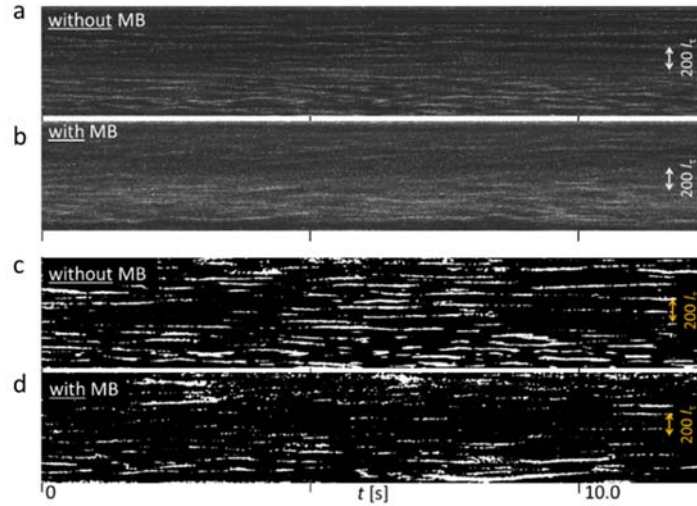
24 A sample snapshot of image is shown in **Fig. 4c**, which is the case without microbubble injection. There  
25 can be seen a stripe pattern as expected. Thick and thin bands mixed in the image correspond to the  
26 arrangement of stream-wise vortices. Since low-speed streaks exist at the center of paired stream-wise  
27 vortices, span-wise spacing of the low-speed streaks can be evaluated by image processing. It must be  
28 reminded that the flake concentration is almost uniform anywhere including outside of the boundary layer.  
29 Thus, individual dots visible in the image do not express the simple presence of the flake but they inform the  
30 structure of liquid phase with the number density of the dots.



1  
 2 **Fig. 4** Visualization of turbulent coherent structure using flake; (a) microscope image of Kalliroscope taken  
 3 by the authors, (b) laser reflection pattern and (c) a sample snapshot in absent of microbubbles

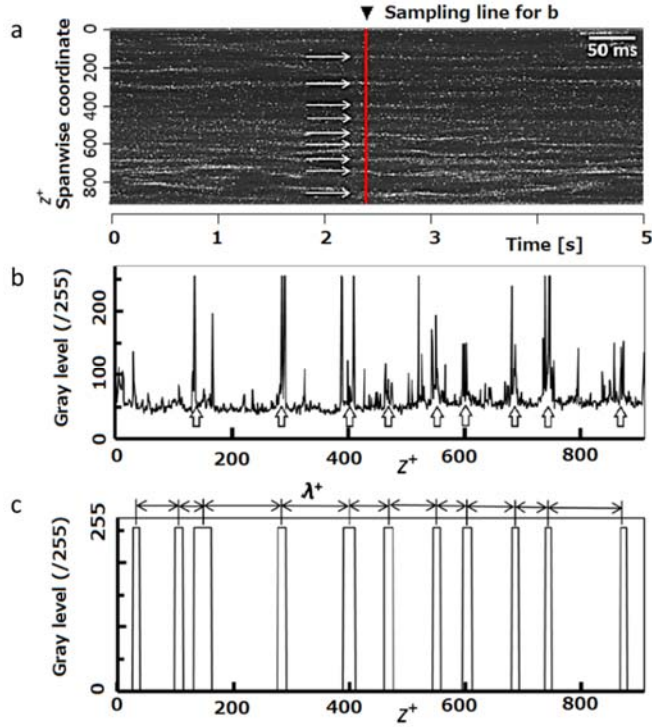
4 **3-2. Quantitative analysis**

5 **Fig. 5** depicts time-line blow up image of the flake reflection at  $Re_x = 2.00 \times 10^4$  ( $x = 281$  mm). It is sampled  
 6 from high-speed video camera movie on a span-wise segment ( $1 \times 1024$  pixels) at the center of the frame.  
 7 Abscissa and ordinate indicate the time, and the span-wise coordinate, i.e. each panel expresses spatio-  
 8 temporal distribution of stream-wise vortices. Known spacing of the low-speed streaks in single phase  
 9 boundary layer is about  $200l_\tau$ , which coincides with doubled spacing of the visible stripe in the figures, i.e. a  
 10 pair of stream-wise vortices corresponds to a single low-speed streak between them. To measure these spacing,  
 11 the time-line images are binarized by a threshold considering averaged brightness, and low-pass filtered by  
 12 a two-dimensional median filter whose radius is approximately  $9l_\tau$  (10 pixels). The binarized images are  
 13 presented in **Fig. 5c** and **5d**, in which white blobs indicate stream-wise vortices extracted.



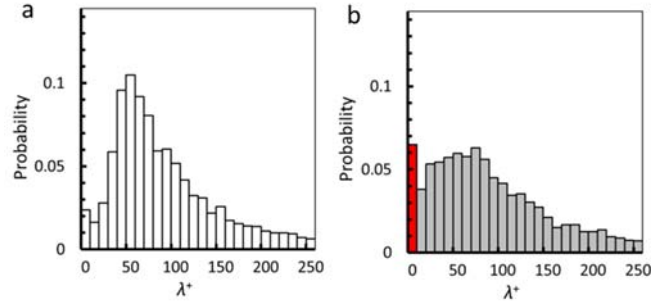
1  
 2 **Fig. 5** Time-line blow up image of near-wall turbulent eddies visualized by micro grossy flake; (a) original  
 3 image in the case without microbubble injection, (b) that with microbubble injection, (c) binarized image  
 4 in the case without microbubble injection and (d) that with microbubble injection.

5 **Fig. 6** shows how the spacing of low-speed streaks is measured by image processing. In the figure, the  
 6 spanwise coordinate is normalized by the wall unit,  $z^+ = z/l_\tau$ . A gray level profile along the red line in **Fig. 6a**  
 7 is shown in **Fig. 6b** which involves many spiky peaks coming out due to light scattering of individual flakes,  
 8 and most of them are much narrower than  $40l_\tau$ . Since such a small eddy does not exist in theory, we convert  
 9 the profile using a threshold to **Fig. 6c** in which individual locations of streamwise vortices and low-speed  
 10 streaks become identifiable.



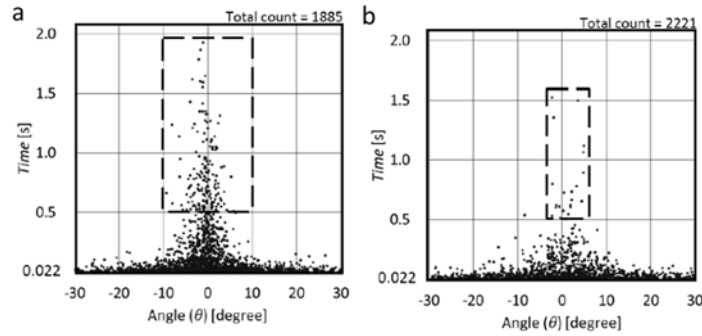
1  
2 **Fig. 6** Brightness profile of turbulent eddies visualized by flake; (a) time-line blow up image, (b)  
3 instantaneous brightness profile and (c) binarized profile of the brightness to extract locations of  
4 streamwise vortices and low-speed streaks

5 From the binarized profile, local interval of the low-speed streaks  $\lambda^+$  is measured for all the sampling  
6 period of 19 s using 9500 frames, and counted as a relative frequency histogram as shown in **Fig. 7**. The peak  
7 within the range of  $50 \leq \lambda^+ < 60$  in the case without microbubble (**Fig. 7a**) corresponds to the half value of  
8 the mean spacing between two low-speed streaks and agrees with past studies [29, 30]. In contrast, the  
9 histogram with microbubble additive takes a blunt peak in the range of  $70 \leq \lambda^+ < 80$ , indicating span-wise  
10 elongation of coherent structures. Here, the near-zero peak detected at  $0 \leq \lambda^+ < 10$  (the red bar in **Fig. 7b**)  
11 comes from the noise caused by dot-wise scattering of laser light on microbubbles, irrelevantly to coherent  
12 structures, and can be ignored. Average value of the spacing  $\overline{\lambda^+}$  is obtained to be 107 in the case without  
13 microbubbles, and that with microbubbles is measured to be 132. The increase means a structural elongation  
14 of near wall turbulence at 23.4%, and infers with Eq. (8) that the wall friction is reduced by 34.3%.



1  
 2 **Fig. 7** Spanwise spacing of turbulent eddies measured from micro glossy flake visualization; (a) turbulent  
 3 boundary layer without microbubbles and (b) the one with microbubble additive.

4 Finally, **Fig. 8** represents measured relationship between visible lifetime of stream-wise vortices,  $T$ , and tilt  
 5 angle of their principal axis from main flow direction,  $\theta$  ( $-90^\circ \leq \theta \leq 90^\circ$ ). Comparing the data between the  
 6 two cases, occurrence frequency of stream-wise vortices is reduced with adding microbubbles while eddies  
 7 with short code length survive. This trend qualitatively agrees with past studies [34, 35] which found collapse  
 8 of turbulent coherent structures and reduction of Reynolds shear stress due to mixture of microbubbles.



9  
 10 **Fig. 8** Visible life time and tilting angle of streamwise vortices; (a) without microbubbles and (b) with  
 11 microbubbles

#### 12 4. Rainbow illumination of microbubble clouds

13 Considering of size of the turbulent vortices, almost  $50l_\tau$ , this indicates that individual microbubbles cannot  
 14 create liquid flow in their spatial scales to destroy turbulent vortices. Instead, formation of microbubble  
 15 clouds much larger than the wall unit can alter the coherent structures in inertia region. Particles and bubbles  
 16 in the turbulence are affected by the turbulence eddies and their spatial distribution is modified [36–38].

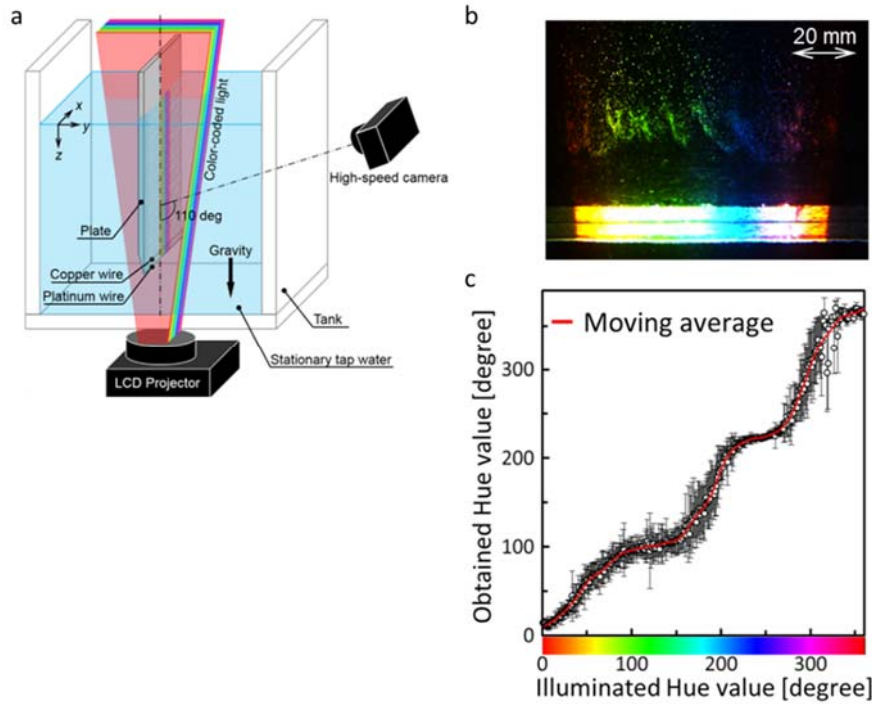
17 In this section, we introduce a method for visualizing microbubble clouds by rainbow illumination and  
 18 investigate spatial distribution of microbubbles in the boundary layer. Basic idea of rainbow illumination is  
 19 similar to color-coded 3-D particle tracking velocimetry for identifying tracer particles [24]. In such a PTV,

1 the out-of-plane coordinate of individual particle is estimated from hue value of the colored particles to be  
2 combined with two in-plane coordinates. In application to microbubbles' coloring, difference arises due to  
3 unique optical characteristics of spherical gas–liquid interface as explained below.

#### 4 **4-1. Hue characteristics of scattering light from microbubbles**

5 Natural rainbow in atmosphere emerges due to spherical water droplets scattering light in slightly different  
6 direction dependent on wavelength of the light. In cases of microbubbles in water, similar phenomenon  
7 occurs in white lighting, which leaves pseudo color in image plane. In advance of the main experiment, how  
8 microbubbles scatter color-coded light in a quiescent water is investigated using a simple experiment shown  
9 in **Fig. 9**. Schematic diagram of the experiment is presented in **Fig. 9a**. The illuminated color pattern is  
10 controlled by a PC connected to the liquid crystal display projector. In this examination, color is varied in the  
11 span-wise direction of a vertical plate in the water container. A high-speed camera is located outside the  
12 container at  $110^\circ$  to the plate surface, according to the brightest illumination angle of spherical bubbles. A  
13 snapshot recorded by the camera is shown in **Fig. 9b**. By thresholding the brightness value, individual  
14 position of microbubbles and their hue values are obtained as plotted in **Fig. 9c**. Open circles represent  
15 measured hue values with a standard deviation at each position. A red curve in the graph indicates moving  
16 averaged value of the measured data.

17 Ideally, the red curve becomes a linear; illuminated hue values coincide with measured hue values.  
18 Displacement from the linearity originates from two factors. One is microbubble's optical scattering  
19 characteristics dependent on the scattering direction analogous to rainbow principle. Another is light-  
20 receiving characteristic of the camera, which relies on a type of image sensors receiving multi-spectral light  
21 for three primary color bands. This usually brings hue-shift to the three primary colors (red at  $0^\circ$ , green at  
22  $120^\circ$ , blue at  $240^\circ$ ). In addition, there are further minor factors influencing the relationship, such as mutual  
23 light scattering among microbubbles, light attenuation due to overlap of microbubbles in imaging plane, and  
24 digital image compression which does not guarantee conservation of hue value. Regardless to these  
25 influences, the moving averaged curve takes a monotonic function with increase in illuminated hue values.  
26 This allows us to correct measured hue values uniquely and recursively to the original value, and thus, to  
27 determine the position of the microbubbles. For the recursive approach, systematic and random errors are  
28 estimated from local flatness of the moving-averaged curve and local deviation of the plots, respectively.  
29 From the data, maximum error is estimated to be  $20^\circ$  for the both components. This indicates that we classify  
30 whole the domain into 18 ( $= 360^\circ/20^\circ$ ) layers in the depth direction.

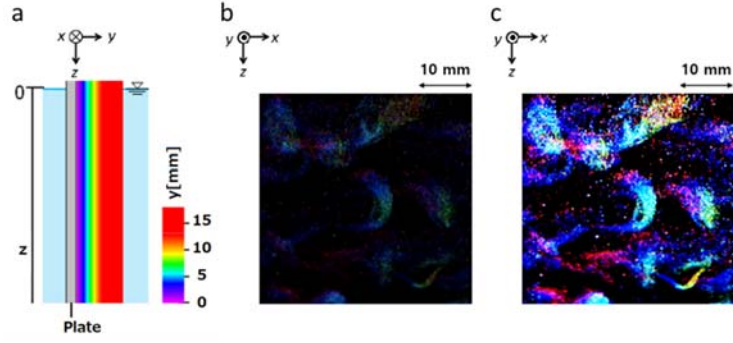


1  
 2 **Fig. 9** A color scattering test of microbubbles; (a) experimental set-up for a color scattering test, (b) a  
 3 snapshot image of hydrogen microbubbles and (c) relationship between illuminated hue and measured  
 4 hue values

#### 5 4-2. Volumetric illumination of boundary layer

6 Learning from the examination, rainbow illumination is applied to the turbulent boundary layer along the test  
 7 plate in the open channel as illustrated in **Fig. 10a**. Hue value is changed linearly to the distance from the  
 8 plate surface on the order of red, magenta, blue, cyan, green, yellow and returning to red. Width of the  
 9 rainbow part is set 12 mm, comparable to the boundary layer thickness. Red monochromatic light is widely  
 10 projected in the outer layer at  $y > 12$  mm (about  $y^+ > 55$ ) so that microbubbles bursting off the boundary layer  
 11 is identified as red color.

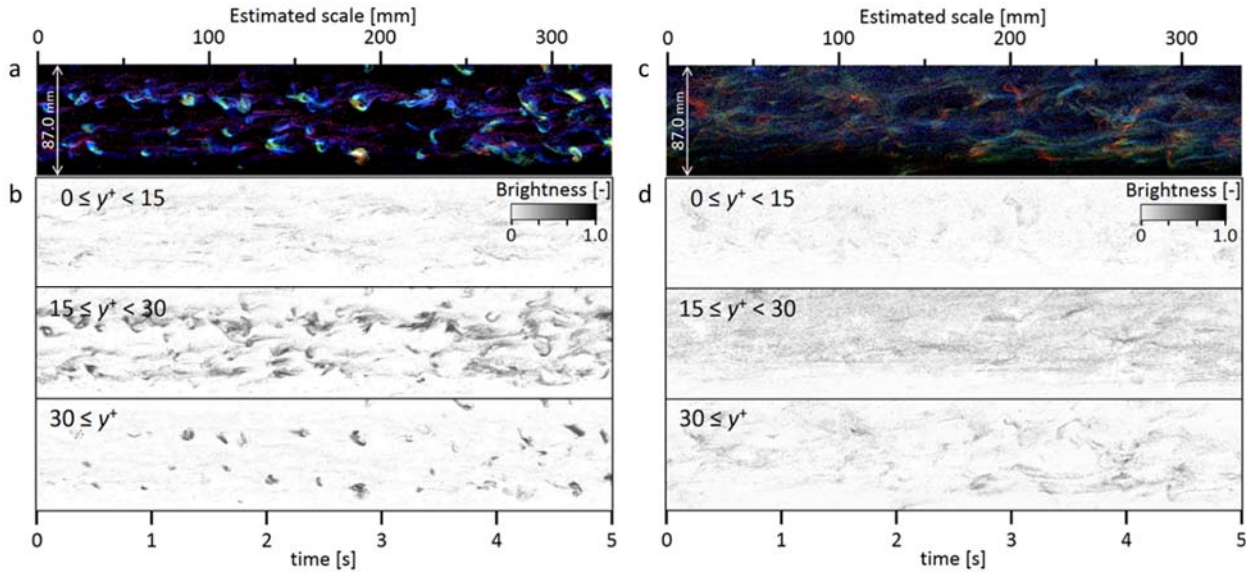
12 An original snapshot of microbubbles image is shown in **Fig. 10b**. The image is regulated dark purposely  
 13 in order to avoid color saturation of image sensors, which has maximum brightness lower than 100 relative  
 14 to 255 brightness level. For easier look in printed manuscript, brightness amplified image of the same  
 15 snapshot is shown in **Fig. 10c**. Cyan dots in the image correspond to microbubbles suspended in wall  
 16 proximity at  $y < 3$  mm (about  $y^+ < 13$ ), while magenta dots are microbubbles accumulated in turbulent eddies  
 17 at  $4 < y < 7$  mm (about  $18 < y^+ < 32$ ). Yellow spots are microbubbles being ejected toward the outer layer at  
 18  $9 < y < 12$  mm (about  $41 < y^+ < 55$ ). It is noted that exact computation of the depth coordinate  $y$  from the  
 19 color image is applied for the original image with hue value conservation but not for the brightness amplified  
 20 image.



1  
2 **Fig. 10** Microbubble visualization by means of color-coded volumetric illumination; (a) tangential projection  
3 of color-coded light, (b) an original sample image of showing hair-pin shaped microbubble clouds and  
4 (c) its brightness amplified image

### 5 4-3. Spatio-temporally resolved distribution

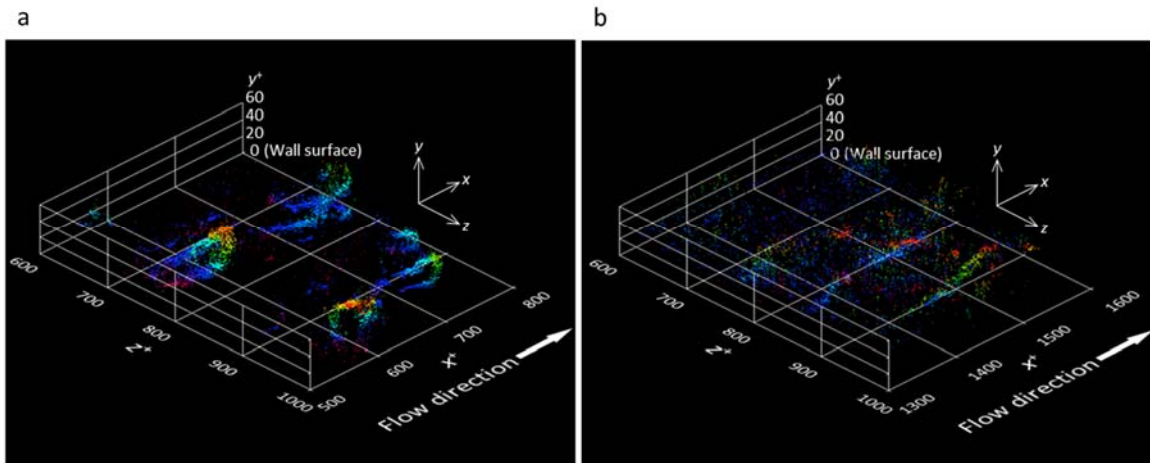
6 By sampling a vertical segment from a movie taken by the high-speed video camera, time-line blow-up  
7 images are generated (**Fig. 11**). In each panel, the horizontal axis indicates time within 5 seconds. The scale  
8 added on the top is an estimated length scale in the stream-wise coordinate according to  $x = U_{mt}$ , with which  
9 spatial wavelength of microbubble clouds is understood.



10  
11 **Fig. 11** Time-line blow up image of colored microbubbles; (a, c) a color image and (b, d) its separated images  
12 to each layer, where (a, b)  $Re_x = 9660$  and (c, d)  $Re_x = 22500$

13 A color image of microbubble distribution recorded at  $Re_x = 9660$  is shown in **Fig. 11a**. By converting  
14 the hue values to  $y$  coordinate, the color time-line blow up images are separated into three layers: viscous  
15 sublayer ( $0 \leq y^+ < 15$ ), buffer layer ( $15 \leq y^+ < 30$ ) and logarithmic layer ( $30 \leq y^+$ ) as shown in **Fig. 11b**, where

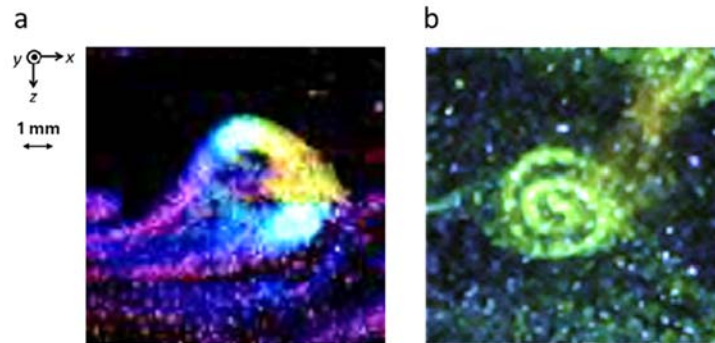
1 wall coordinate is defined by  $y^+ = y/l_\tau$ . The brightness in each layer corresponds to local number density of  
 2 the microbubbles. In the viscous sublayer, microbubbles are distributed with a weak stripe pattern. Span-wise  
 3 spacing of the stripes coincides with that of low-speed streak at this  $Re$  number. Inside the buffer layer,  
 4 microbubbles form localized clouds that have high number density than in the viscous sublayer. It is  
 5 observable that large clouds pass by at a frequency of around 2 Hz, corresponding to 50 mm ( $\sim 220l_\tau$ ) in  
 6 stream-wise interval. In the logarithmic layer, microbubbles come out as spots. These spots are regarded as  
 7 head of each cloud in the buffer layer, conveyed by ejection of liquid phase. In the downstream region at  $Re_x$   
 8 = 22500 (see **Fig. 11c** to **Fig. 11d**), these localized clouds are relatively dispersed all over the layer but most  
 9 of the microbubbles still stay inside each layer. Difference of the cloud formation between the two positions  
 10 is explained by that of enstrophy in liquid phase. That is, liquid phase induces high shear rate in the upstream  
 11 position to rapidly capture the microbubbles in hair-pin shaped vortex cores. To the contrary, the shear rate  
 12 decreases in the downstream region with expanded boundary layer thickness, resulting in calmed cloud  
 13 formation.



14  
 15 **Fig. 12** 3-D depiction of microbubble distribution from hue-to-depth coordinate transform; (a) upstream  
 16 position around  $Re_x = 9660$  and (b) downstream position around  $Re_x = 22500$

17 By the hue-to-depth conversion, 3-D distributions of microbubbles are depicted in **Fig. 12** using the 3-  
 18 D coordinate normalized by wall unit. Color indicates the individual position of microbubbles from the wall.  
 19 At  $Re_x = 9660$ , each cloud has hair-pin shapes stretched in the stream-wise direction. Coherent structures in  
 20 turbulent boundary layer such as ejection, sweep, and low-speed streaks induce these cloud formations.  
 21 Ejection plays a primary role because of the following sequence: ejection collects microbubbles suspended  
 22 in viscous sublayer and conveys them along outward flow to logarithmic layer. In fact, we often found the  
 23 microbubble clouds like in **Fig. 13**. In hair-pin shaped cloud (**Fig. 13a**), local number density of microbubbles  
 24 is estimated to be higher than  $10^4/\text{cm}^3$ , and its volume fraction gets close to the packing limit of spheres. In  
 25 the logarithmic layer, clam-shell shaped clouds often appeared. This infers a long Lagrangian interaction

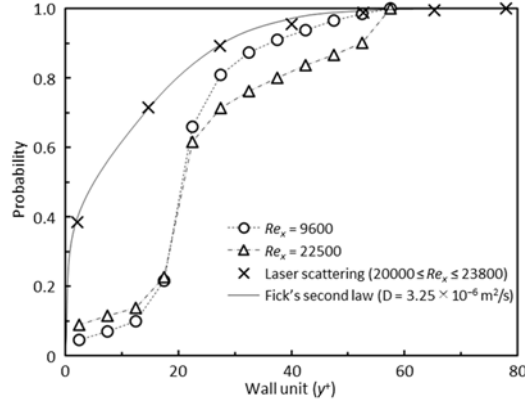
1 experienced between microbubbles and individual eddies. We did not see coalescence of microbubbles even  
2 in these highly dense clouds, of which reason is attributed to rigidity of microbubbles due to strong surface  
3 tension [15] and also to local repulsion generated by Zeta potential on the microbubble surface in water [39–  
4 42].



5  
6 **Fig. 13** Microbubble clouds observed at  $Re_x = 9660$ ; (a) a hair-pin shaped cloud rising up to the buffer layer  
7 having legs in viscous sublayer and (b) clam shell shaped cloud ejected to logarithmic layer, inferring  
8 long Lagrangian interaction between microbubbles and individual eddies

#### 9 4-4. Averaged concentration profiles

10 To evaluate bulk turbulent diffusivity of the microbubbles, time-averaged concentration profile is measured.  
11 **Fig. 14** represents the cumulative histograms of microbubble clouds, which is a bubble-presence probability  
12 integrated in  $y$  direction. The value takes 0 at  $y = 0$ , and unity at infinity far from the wall. Circle and triangular  
13 symbols in the graph are measured from the rainbow visualization at two different  $Re_x$  numbers. Cross  
14 symbols are the data measured by a single laser-sheet illumination of microbubbles with traversing the  $y$   
15 coordinate (see **Fig. 3a**).



1  
2 **Fig. 14** Cumulative frequency histogram of microbubble concentration profile inside the turbulent boundary  
3 layer measured by color-coded illumination and laser scattering methods.

4 The curve fitting the cross symbols is the value according to Fick's second law assuming a constant  
5 diffusivity of microbubbles as the simplest model. The curve is obtained using the following one-dimensional  
6 diffusion equation for a concentration profile;

$$7 \quad \frac{\partial C}{\partial t} = D \frac{\partial^2 C}{\partial y^2}, \quad (9)$$

8 where  $C(y, t)$  is the concentration of microbubbles, and  $D$  denotes the microbubble diffusivity with a  
9 dimension of  $m^2/s$ . As giving  $C(y, 0)$  a delta function at  $y = 0$ , Eq. (9) gives universal solution as

$$10 \quad C(y, t) = \frac{1}{2\sqrt{\pi Dt}} \exp\left(-\frac{y^2}{4Dt}\right). \quad (10)$$

11 Substituting present experimental conditions such as  $t = x/U_m$  into Eq. (10), the most matched profile with  
12 experimental data is derived by changing the diffusivity  $D$ . From least square approach, we have obtained  
13 the microbubble diffusivity as  $D = 3.2 \times 10^{-6} m^2/s$ . This value is larger than kinematic viscosity of water,  $\nu =$   
14  $0.9 \times 10^{-6} m^2/s$  in present experiment, indicating active diffusion of microbubbles more than molecular  
15 momentum diffusivity of water. Effective Schmidt number of microbubbles is hence estimated as  $Sc = \nu/D =$   
16  $0.31$ . In contrast, turbulent momentum diffusivity is estimated as  $\nu_t = l_\tau U_m = 1.49 \times 10^{-5} m^2/s$  on the present  
17 liquid flow condition. Thus, the relative diffusivity of microbubbles is  $D/\nu_t = 0.21$ , being sufficiently smaller  
18 than unity. This tells that microbubbles tend to stay inside the turbulent boundary layer relatively to the  
19 expansion of the boundary layer thickness in  $y$  direction. The trend can be also confirmed in **Fig. 14** that 90%  
20 of microbubbles are concentrated inside the wall-closest layer of  $0 < y^+ < 30$ . Such reduced diffusion effect  
21 of microbubbles against turbulence is attributed to cloud formation inside the buffer layer where  
22 microbubbles are captured into vortex cores. Accumulation and diffusion of small dispersion in turbulence is  
23 generally explained by crossing trajectories of the dispersion to individual eddies [36, 43, 44]. It is  
24 indisputable that primary force to accumulate microbubbles into vortex cores is local pressure gradient, i.e.

1 high enstrophy inside the vortices. Lift force of spherical microbubbles with small vertical slip also assists  
 2 their accumulation; here lift acts in Saffman regime because of  $Re_b < 1$ , and orients toward the wall.

3 Another point found from the data is the difference of the profile between laser scattering measurement  
 4 and rainbow illumination. The rainbow illumination underestimates the cumulative histogram at  $0 < y^+ < 60$ .  
 5 This is due to optical occlusion of microbubbles as microbubbles form high-density clouds. Microbubbles  
 6 existing under microbubble clouds cannot be counted by the rainbow illumination. This is regarded as  
 7 disadvantage of the rainbow illumination, however, it also infers that the gap between two measurements  
 8 proves generation of microbubble clouds in the corresponding layer. Since the cumulative histogram steeply  
 9 recovers at  $20 < y^+ < 30$ , it is understood that dense microbubble clouds are actively induced mainly in the  
 10 buffer layer. This fact is reasonable since enstrophy takes the highest value inside the buffer layer to produce  
 11 slip velocity between two phases.

## 12 5. Discussions

13 Why can microbubbles alter the coherent structures of wall turbulence so sensitively? Only at 0.01% of  
 14 microbubble volume fraction given to the boundary layer, we confirmed visible modification of the inner  
 15 layer structure leading to 34% of drag reduction. Note that this drag reduction is not directly measured value  
 16 and just estimated value from the increasing average space between streaks with microbubbles. Similar  
 17 impact at 0.03% of microbubble volume fraction was reported by Hara *et al.* [23] who confirmed 30% of  
 18 drag reduction. They conducted PTV measurement and found local Reynolds shear stress reduced only inside  
 19 the buffer layer. For volume fraction larger than 0.2%, Serizawa *et al.* [45] and Shattet *et al.* [22] reported re-  
 20 laminarization of pipe flows as viewed from measured pipe friction factors in a turbulent flow transition  
 21 regime. At further higher volume fraction over 2%, volumetric impact of microbubbles starts to dominate as  
 22 reported by Ferrante and Elghobashi [46] using DNS and Zhen and Hassan [20] by PIV. Back to the first  
 23 question, we attempt to derive the most possible reason which survives at dilute limit of microbubbles one-  
 24 by-one as below.

### 25 5-1. High interfacial concentration

26 Even though volume fraction of microbubble is controlled low, total area of gas-liquid interface is provided  
 27 very high. To quantify this effect, following quantity can represent dimensionless interfacial concentration  
 28 as a mean value inside the boundary layer:

$$29 \quad \beta = \pi d^2 \frac{N}{WL} = \frac{6\delta}{d} \alpha, \quad \therefore \alpha = \frac{N}{WL\delta} \frac{\pi d^3}{6}, \quad (11)$$

30 where  $\alpha$  is void fraction inside the boundary layer defined by the span-wise length  $W$ , the stream-wise length  
 31  $L$ , and the boundary layer thickness  $\delta$ . Here,  $d$  and  $N$  stand for the microbubble diameter and the number of

1 microbubbles in the volume of  $LW\delta$ . The quantity  $\beta$  indicates the ratio of total microbubble interfacial area  
 2 inside boundary layer to the area of wall surface. In the present flow condition, Eq. (11) becomes  $\beta = 2400\alpha$   
 3 at  $\delta = 12$  mm and  $d = 30$   $\mu\text{m}$ . Thus,  $\alpha = 0.01\%$  provides  $\beta = 24\%$ . This is superficially equivalent to the wall  
 4 occupied by gas film at 24%. Since momentum exchange between two phases in Stokes drag regime increases  
 5 proportionally to the interfacial area concentration, the parameter could be an appropriate factor to explain  
 6 the magnitude of the microbubbles' impact on the modification of coherent structures in the turbulent  
 7 boundary layer.

## 8 5-2. Buoyancy in localized state

9 Buoyant force of microbubbles acts on liquid flow in proportion to the microbubble volume fraction. Impact  
 10 of the buoyant force to the liquid flow can be estimated by the ratio of buoyant potential  $E_b$  to kinetic energy  
 11 of liquid flow  $E_l$  inside the boundary layer as

$$12 \quad \varepsilon = \frac{E_b}{E_l} = \frac{N\rho g\pi d^3 / 6}{W \int_0^\delta \frac{1}{2} \rho u^{-2}(y) dy} = \frac{9\alpha g\delta}{7U_m^2}, \quad (12)$$

13 where primitive parameters in the definition are the same as previous ones. In the present flow condition, Eq.  
 14 (12) becomes  $\varepsilon = 40\alpha$ , thus  $\varepsilon = 0.4\%$  at  $\alpha = 0.01\%$ . This value is two-order smaller than  $\beta$  estimated in former  
 15 section, but is still significant. Actual impact of buoyancy may be intensified more than Eq. (12) with two  
 16 reasons. One is generation of microbubble clouds taking much higher value of local volume fraction. The  
 17 other is increase of buoyant action to liquid phase as spatial gradient of local volume fraction is given. These  
 18 effects were experimentally confirmed in Taylor–Couette flows, where microbubbles are preferentially  
 19 accumulated to selected locations of vortices [24]. Thus, if denominator of Eq. (12) is replaced with kinetic  
 20 energy of the secondary mode such as primary vortex in shear, the impact becomes one-order higher to be  
 21 comparable to drag reduction rate. In short, localization of microbubble distribution always calls intensified  
 22 buoyant action to coherent structures regardless to Froude number defined in the bulk space.

## 23 5-3. Microbubble cloud rheology

24 As microbubbles form clouds that have high local number density inside, viscosity of the clouds increases  
 25 drastically. Murai *et al.* [47] measured such effective viscosity with around 45% of void fractions using  
 26 interfacial rheometry. Their result is approximated as

$$27 \quad \eta = \frac{\mu_b}{\mu_l} = 1300 \left( \frac{Ca}{10^{-8}} \right)^{-0.45}, \quad Ca = \frac{\mu_l d}{2\sigma} \dot{\gamma}, \quad (13)$$

28 where  $\eta$  is ratio of microbubble cloud viscosity  $\mu_b$  to liquid viscosity  $\mu_l$ .  $Ca$  is capillary number for a single  
 29 microbubble with diameter of  $d$ , interfacial tension of  $\sigma$ , and surrounding liquid shear rate of  $\dot{\gamma}$ . The formula  
 30 is valid only for  $10^{-8} < Ca < 10^{-5}$ , and  $35\% < \alpha < 55\%$ . Substituting the present flow conditions into the  
 31 formula obtains  $Ca = 1.5 \times 10^{-6}$ , and  $\eta = 140$ . For the range of  $\alpha < 35\%$ , the following empirical formula

1 proposed by Mooney [48] is available,

$$2 \quad \eta = \exp\left(\frac{A\alpha}{1-k\alpha}\right), \quad 1.35 < k < 1.91, \quad (14)$$

3 where  $A$  and  $k$  stand for dimensionless parameters describing the frictional impact and spatial arrangement  
4 pattern of spherical dispersion, respectively. Assuming  $k = 1.5$  as a random distribution, coupling of Eq. (13)  
5 and Eq. (14) gives  $A = 6.7$ . Thus, the viscosity ratio takes  $\eta = 38$  at  $\alpha = 30\%$ ,  $\eta = 6.7$  at  $\alpha = 20\%$ , and  $\eta = 2.2$   
6 at  $\alpha = 10\%$ . These values are obviously to explain that microbubble clouds strongly resist to deformation of  
7 fluid. Moreover, we have confirmed that microbubble clouds were induced in vortex cores. This implies the  
8 rheological effect which acts mainly to decay of turbulence.

## 9 **6. Conclusions**

10 In this paper, we reported how microbubbles interact with eddies in a spatially developing turbulent boundary  
11 layer along a flat wall. We have adapted a rainbow visualization technique to explore microbubbles'  
12 preferential concentration into low-speed streak regions close to the viscous sublayer and into hair-pin shaped  
13 clouds in the buffer layer. These accumulations provided reduced diffusion effect of microbubbles as proved  
14 by microbubble Schmidt number that was obtained smaller than unity. We also visualized turbulent eddies in  
15 the liquid phase with flake optics, and confirmed a significant elongation of span-wise spacing of low-speed  
16 streaks and also a reduction of occurrence frequency of long stream-wise vortices. In the final part, we tried  
17 to offer the reason why only 0.01% of microbubble volume fraction can cause clearly visible alternation of  
18 the coherent structure. It is mainly attributed to effect of microbubble clouds on interfacial concentration,  
19 localized buoyancy, and effective viscosity. While some of them still need further experimental proving, we  
20 expect that the present experimental results re-accelerate the study of microbubble drag reduction.

## 21 **Acknowledgments**

22 The work presented in the manuscript was supported by JSPS KAKENHI grant nos. 17H01245 and  
23 17K14583, and Innovative Science & Technology Initiative for Security, ATLA, Japan. Also the authors  
24 express thanks to Mr. Toshiyuki Sampo, Dr. Yoshiaki Takahashi.

## 25 **References**

- 26 [1] M. McCormick, R. Bhattacharyya, Drag reduction of a submersible hull by electrolysis, *Nav. Eng. J.* 85  
27 (1973) 11–16.
- 28 [2] H.H. Legner, Simple model for gas bubble drag reduction, *Phys. Fluids* 27 (1984) 2788–2790.
- 29 [3] J.L. Marie, A simple analytical formulation for microbubble drag reduction, *PhysicoChemical*  
30 *Hydrodynamics* 8 (1987) 213–220.

- 1 [4] C.L. Merkle, S. Deutsch, Drag reduction in liquid boundary layers by gas injection, *Prog. Astronaut.*  
2 *Aeronaut.* 123 (1990) 351–411.
- 3 [5] C.L. Merkle, S. Deutsch, Microbubble drag reduction in liquid turbulent boundary layers, *ASME Appl.*  
4 *Mech. Rev.* 45 (1992) 103–127.
- 5 [6] H. Kato, T. Iwashina, M. Miyanaga, H. Yamaguchi, Effect of microbubbles on the structure of turbulence  
6 in a turbulent boundary layer, *J. Mar. Sci. Tech.* 4 (1999) 115–162.
- 7 [7] Y. Kodama, A. Kakugawa, T. Takahashi, H. Kawashima, Experimental study on microbubbles and their  
8 applicability to ships for skin friction reduction, *Int. J. Heat Fluid Flow*, 21 (2000) 582–588.
- 9 [8] Y. Moriguchi, H. Kato, Influence of microbubble diameter and distribution on frictional resistance  
10 reduction, *J. Mar. Sci. Tech.* 7 (2002) 79–85.
- 11 [9] A. Kitagawa, K. Hishida, Y. Kodama, Flow structure of microbubble-laden turbulent channel flow  
12 measured by PIV combined with the shadow image technique, *Exp. Fluids* 38 (2005) 466–475.
- 13 [10] Y. Tasaka, T. Kimura, Y. Murai, Estimating the effective viscosity of bubble suspensions in oscillatory  
14 shear flows by means of ultrasonic spinning rheometry, *Exp. Fluids* 56 (2015) 1867.
- 15 [11] D.P.M. van Gils, D.N. Guzman, C. Sun, D. Lohse, The importance of bubble deformability for strong  
16 drag reduction in bubbly turbulent Taylor–Couette flow, *J. Fluids Mech.* 722 (2013) 317–347.
- 17 [12] H.J. Park, Y. Tasaka, Y. Murai, Bubbly drag reduction investigated by time-resolved ultrasonic pulse  
18 echography for liquid films creeping inside a turbulent boundary layer, *Exp. Therm. Fluid Sci.* 103  
19 (2019) 66–77.
- 20 [13] A. Kitagawa, P. Denissenko, Y. Murai, Behavior of bubbles moving along horizontal flat plates with  
21 different surface wettability, *Exp. Therm. Fluid Sci.* 104 (2019) 141–152.
- 22 [14] A. Ferrante, S. Elghobashi, On the physical mechanism of drag reduction in a spatially developing  
23 turbulent boundary layer laden with microbubbles, *J. Fluid Mech.* 503 (2004) 345–355.
- 24 [15] Y. Murai, T. Shiratori, I. Kumagai, P. A. Ruehs, P. Fischer, Effective viscosity measurement of interfacial  
25 bubble and particle layers at high volume fraction, *Flow Meas. Instrum.* 41 (2016) 121–128.
- 26 [16] Y. Tasaka, Y. Yoshida, R. Rapberger, Y. Murai, Linear viscoelastic analysis using frequency-domain  
27 algorithm on oscillating circular shear flows for bubble suspensions, *Rheologica Acta* 57 (2018) 229–  
28 240.
- 29 [17] T. Watamura, A. Kitagawa, Y. Murai, Cloud clustering of microbubbles ascending along a vertical wall  
30 proximity, *Chem. Eng. Sci.* 208 (2019) 115132.
- 31 [18] V. Mathai, E. Calzavarini, J. Brons, C. Sun, D. Lohse, Microbubbles and microparticles are not faithful  
32 tracers of turbulent acceleration. *Phys. Rev. Lett.* 117 (2016) 024501.

- 1 [19] Y. Murai, Y. Oishi, Y. Takeda, F. Yamamoto, Turbulent shear stress profiles in a bubbly channel flow  
2 assessed by particle tracking velocimetry, *Exp. Fluids* 41 (2006) 343–352.
- 3 [20] L. Zhen, Y.A. Hassan, Wavelet autocorrelation identification of the turbulent flow multi-scales for drag  
4 reduction process in microbubbly flows, *Chem. Eng. Sci.* 61 (2006) 7107–7114.
- 5 [21] Y. Murai, H. Oiwa, Y. Takeda, Frictional drag reduction in bubbly Couette–Taylor flow, *Phys. Fluids* 20  
6 (2008) 034101.
- 7 [22] M.M.E. Shatat, S. Yanase, T. Takami, T. Hyakutake, Drag Reduction Effects of Micro-Bubbles in  
8 Straight and Helical Pipes, *J. Fluid Sci. Tech.* 4 (2009) 156–167.
- 9 [23] K. Hara, T. Suzuki, F. Yamamoto, Image analysis applied to study on frictional drag reduction by  
10 electrolytic microbubbles in a turbulent channel flow, *Exp. Fluids* 50 (2011) 715–727.
- 11 [24] T. Watamura, Y. Tasaka, Y. Murai, Intensified and attenuated waves in a microbubble Taylor–Couette  
12 flow, *Phys. Fluids* 25 (2013) 054107.
- 13 [25] J. Xiong, R. Idoughi, A.A. Aguirre–Pablo, A.B. Aljedaani, X. Dun, Q. Fu, S.T. Thoroddsen, W. Heidrich,  
14 Rainbow particle imaging velocimetry for dense 3D fluid velocity imaging, *ACM Trans. Graph.* 36  
15 (2017) 36.
- 16 [26] P. Matisse, M. Gorman, Neutrally buoyant anisotropic particles for flow visualization, *Phys. Fluids* 27  
17 (1984) 759.
- 18 [27] J. Ohkubo, Y. Tasaka, H.J. Park, Y. Murai, Extraction of 3D vortex structures from a turbulent puff in a  
19 pipe using two-color illumination and flakes, *J. vis.* 19 (2016) 643–651.
- 20 [28] W. Cheng, Y. Murai, T. Sasaki, F. Yamamoto, Bubble velocity measurement with a recursive cross  
21 correlation PIV technique, *Flow Meas. Instrum.* 16 (2005) 35–46.
- 22 [29] C.R. Smith, S.P. Metzler, The characteristics of low-speed streaks in the near-wall region of a turbulent  
23 boundary layer, *J. Fluid Mech.* 129 (1983) 27–54.
- 24 [30] M. Zacksenhouse, G. Abramovich, G. Hetsroni, Automatic spatial characterization of low-speed streaks  
25 from thermal images, *Exp. Fluids* 31 (2001) 229–239.
- 26 [31] E.K. Longmire, I. Marusic, S. Pothos, Dual-plane PIV technique to determine the complete velocity  
27 gradient tensor in a turbulent boundary layer, *Exp. Fluids* 39 (2005) 222–231.
- 28 [32] S. Robinson, Coherent Motions in the turbulent boundary layer, *Annu. Rev. Fluid Mech.* 23 (1991) 601–  
29 639.
- 30 [33] H.J. Park, Y. Tasaka, Y. Murai, Vortical structures swept by a bubble swarm in turbulent boundary layers,  
31 *Chem. Eng. Sci.* 116 (2014) 486–496.
- 32 [34] Y. Oishi, Y. Murai, Y. Tasaka, Y. Takeda, Motion of Microbubbles Relative to Streamwise Vortices in

- 1 the Wall Turbulence, 6th Int. Conf. Multiphase Flow (2007) 535.
- 2 [35] C.C. Gutierrez–Torres, Y.A. Hassan, J.A. Jimenez–Bernal, Turbulence structure modification and drag  
3 reduction by microbubble injections in a boundary layer channel flow, *J. Fluids Eng.* 130 (2008) 111304.
- 4 [36] M. R. Maxey, The gravitational setting of aerosol particles in homogeneous turbulence and random flow  
5 fields, *J. Fluid Mech.* 174 (1987) 441–645.
- 6 [37] H. Parishani, O. Ayala, B. Rosa, L.-P. Wang, W.W. Grabowski, Effects of gravity on the acceleration  
7 and pair statistics of inertial particles in homogeneous isotropic turbulence, *Phys. Fluids* 27 (2015)  
8 033304.
- 9 [38] V. Mathai, S.G. Huisman, C. Sun, D. Lohse, M. Bourgoïn, Dispersion of air bubbles in isotropic  
10 turbulence, *Phys. Rev. Lett.* 121 (2018) 054501.
- 11 [39] S. Usui, H. Sasaki, H. Matsukawa, The dependence of Zeta potential on bubble size as determined by  
12 the Dorn effect, *J. Colloid Interface Sci.* 81 (1981) 80–84.
- 13 [40] R.H. Yoon, J.L. Yordan, Zeta potential measurements on microbubbles generated using various  
14 surfactants, *J. Colloid Interface Sci.* 113 (1986) 430–438.
- 15 [41] M. Takahashi, Zeta potential of microbubbles in aqueous solutions – electrical properties of the gas-  
16 liquid interface, *J. Phys. Chem.* 109 (2005) 21858–21864.
- 17 [42] F.Y. Ushikubo, M. Enari, T. Furukawa, R. Nakagawa, Y. Makino, Y. Kawagoe, S. Oshita, Zeta-potential  
18 of Micro- and/or Nano-bubbles in Water Produced by Some Kinds of Gases, *IFAC Proc. Vol.* 43 (2010)  
19 283–288.
- 20 [43] F. Risso, Agitation, Mixing, and Transfers Induced by Bubbles, *Annu. Rev. Fluid Mech.* 50 (2018) 25–  
21 48.
- 22 [44] E. Alméras, V. Mathai, C. Sun, D. Lohse, Mixing induced by a bubble swarm rising through incident  
23 turbulence, *Int. J. Multiphase Flow* 114 (2019) 316–322.
- 24 [45] A. Serizawa, T. Inui, T. Eguchi, Flow characteristics and pseudo-laminarization of vertically upward  
25 air-water milky bubbly flow with micro bubbles in a pipe, *Jpn. J. Multiphase Flow* 19 (2005) 335–340  
26 (in Japanese).
- 27 [46] A. Ferrante, S. Elghobashi, Reynolds number effect on drag reduction in a microbubble- laden spatially  
28 developing turbulent boundary layer, *J. Fluid Mech.* 543 (2005) 93–106.
- 29 [47] Y. Murai, T. Shiratori, I. Kumagai, P.A. Ruehs, P. Fischer, Effective viscosity measurement of interfacial  
30 bubble and particle layers at high volume fraction, *Flow Meas. Instrum.* 41 (2015) 121–128.
- 31 [48] M. Mooney, The viscosity of a concentrated suspension of spherical particles, *J. Colloid Sci.* 6 (1951)  
32 162–170.